Geophysical Journal International

Geophys. J. Int. (2019) **219,** 1405–1420 doi: 10.1093/gji/ggz351
Advance Access publication 2019 September 05
GJI Seismology

Validation of a fast semi-analytic method for surface-wave propagation in layered media

Quentin Brissaud[1] and Victor C. Tsai[2]

[1]*Department of Geophysics, Seismological Laboratory, California Institute of Technology, 1200 E California Blvd, Pasadena, CA 91125, USA.*
E-mail: quentinb@caltech.edu
[2]*Department of Earth, Environmental and Planetary Sciences, Brown university, Providence, Rhode Island 02912, USA.*

Accepted 2019 September 2. Received 2019 May 17; in original form 2019 January 30

SUMMARY

Green's functions provide an efficient way to model surface-wave propagation and estimate physical quantities for near-surface processes. Several surface-wave Green's function approximations (far-field, no mode conversions and no higher mode surface waves) have been employed for numerous applications such as estimating sediment flux in rivers, determining the properties of landslides, identifying the seismic signature of debris flows or to study seismic noise through cross-correlations. Based on those approximations, simple empirical scalings exist to derive phase velocities and amplitudes for pure power-law velocity structures providing an exact relationship between the velocity model and the Green's functions. However, no quantitative estimates of the accuracy of these simple scalings have been reported for impulsive sources in complex velocity structures. In this paper, we address this gap by comparing the theoretical predictions to high-order numerical solutions for the vertical component of the wavefield. The Green's functions computation shows that attenuation-induced dispersion of phase and group velocity plays an important role and should be carefully taken into account to correctly describe how surface-wave amplitudes decay with distance. The comparisons confirm the general reliability of the semi-analytic model for power-law and realistic shear velocity structures to describe fundamental-mode Rayleigh waves in terms of characteristic frequencies, amplitudes and envelopes. At short distances from the source, and for large near-surface velocity gradients or high Q values, the low-frequency energy can be dominated by higher mode surface waves that can be captured by introducing additional higher mode Rayleigh-wave power-law scalings. We also find that the energy spectral density for realistic shear-velocity models close to piecewise power-law models can be accurately modelled using the same non-dimensional scalings. The frequency range of validity of each power-law scaling can be derived from the corresponding phase velocities. Finally, highly discontinuous near-surface velocity profiles can also be approximated by a combination of power-law scalings. Analytical Green's functions derived from the non-dimensionalization provide a good estimate of the amplitude and variations of the energy distribution, although the predictions are quite poor around the frequency bounds of each power-law scaling.

Key words: Numerical approximations and analysis; Seismic noise; Surface waves and free oscillations; Wave propagation.

1 INTRODUCTION

The modelling of seismic surface waves is a critical step in many near-surface process studies that are based on ground motion observations (debris flows, landslides, glaciers, rivers and volcanic tremor; Bard *et al.* 1999; Tsai & Ekström 2007; Burtin *et al.* 2008; McNutt & Nishimura 2008; Tsai *et al.* 2012; Lai *et al.* 2018), ambient noise cross-correlation applications (Knopoff 1937; Xia *et al.* 1999; Rivet *et al.* 2015; Tomar *et al.* 2018) and seismic hazard assessment applications (Bonnefoy-Claudet *et al.* 2006; Perron *et al.* 2018). The seismic analysis of surface processes and the interpretation of seismic field observations rely on our ability to accurately model surface-wave propagation in heterogeneous media (Larose *et al.* 2015). Surface-wave propagation is frequently computed using various Green's functions approximations (Aki & Richards 1980) as they offer a concise and computationally inexpensive representation of the wavefield (Tsai & Atiganyanun 2014) compared to more sophisticated full-wave numerical methods (e.g. finite differences or finite elements).

The analytic relationship between a velocity model and the Rayleigh-wave energy spectrum provided by Green's functions can prove to be useful to derive simple physics-based wave-propagation models (Tsai *et al.* 2012; Gimbert *et al.* 2014; Lai *et al.* 2018) and to perform the associated inversion. However, their computation traditionally relies on a numerical integration of the differential motion–stress equations (Aki & Richards 1980, ch. 7.2.1) implemented in various publicly available software (Herrmann 2013; Haney & Tsai 2017). In Tsai & Atiganyanun (2014), the authors showed that the non-dimensionalization of the Rayleigh-wave governing equations for pure 1-D power-law structures results in an exact expression that links the shear-velocity power-law parameters to the Green's function amplitude and the associated phase and group velocities. Even though the near-surface geological structure is extremely complex, piecewise power-law velocity models can provide a good approximation at low frequencies (Boore & Joyner 1997), the structure at high frequencies being poorly constrained. For more complex velocity structures, which can be approximated by piecewise power laws, the frequency transition between each power-law scaling tends to occur when phase velocities cross. It seems, therefore, possible to represent the Rayleigh-wave energy spectrum using the non-dimensional approach even in highly heterogeneous media.

Any Green's functions description relies on various assumptions about wave propagation: a point source approximation, receivers located in the far-field and no lateral discontinuities. While, lateral discontinuities and the associated seismic-wave diffraction and conversions (Yanovskaya *et al.* 2012) can generally be neglected at short distances from the source or for large wavelengths, the interaction between surface and body waves and the propagation of higher mode surface waves can have a strong impact on the wavefield in discontinuous media but are generally ignored (Bonnefoy-Claudet *et al.* 2006). Finally, the non-dimensional scalings described above are only valid for pure power laws, while more realistic velocity structures will introduce more complexity, so one can question the range of validity of the approximations in discontinuous media for surface-wave propagation, a question that, to the best of our knowledge, has not been answered in the past.

Herein, we aim to provide some quantitative estimates of the accuracy of semi-analytic Green's functions computed through the non-dimensionalization introduced in Tsai & Atiganyanun (2014) for complex 1-D media and give a better understanding of the method's limitation. In heterogeneous media and for arbitrary sources, the surface wavefield can be composed of both Love and Rayleigh waves. In order to avoid accounting for both contributions and running expensive full 3-D simulations, we only consider vertical forces in this paper, that is, we focus on Rayleigh waves. Although for arbitrary sources Love waves can dominate the horizontal energy distribution (Bonnefoy-Claudet *et al.* 2006), Rayleigh-wave dispersion curves are widely used for near-surface characterization (e.g. Tomar *et al.* 2018) or to study specific underlying processes that cause seismic noise due to vertical-component ground motions generally being more reliable (e.g. Gimbert *et al.* 2014). Since limited field observations exist for which the seismic structure is well constrained, we assess the reliability of semi-analytic Green's functions by comparison with high-order numerical solutions that accurately represent wave propagation in complex realistic media. We first summarize the main analytic results that we aim to assess as well as the numerical method to generate reference solutions. Then, we compare results for a range of seismic media with increasing structural complexity to study the impact of attenuation and shear-velocity depth gradients on wave propagation for idealized sedimentary basin seismic models. Finally, we consider a realistic piecewise power-law model and 1-D profiles extracted from the SCEC Community Velocity Model (CVM-S4.26, Lee *et al.* 2014) to investigate the influence of strong shear-velocity discontinuities on the energy distribution and assess the accuracy of the semi-analytic approach.

2 SPECTRAL ENERGY PREDICTED BY ANALYTIC GREEN'S FUNCTIONS

In this section, we recall the main theoretical results to derive the vertical energy distribution for linear wave propagation due to an impulsive source using semi-analytic Green's functions. From Aki & Richards (1980; ch. 7), the spectral ground velocity amplitude $|\dot{u}(f, r)|$ ($\mathrm{m\,s^{-1}\,Hz^{-1}}$) for a given frequency f (Hz) and at a distance r (m) from the source, can be expressed as

$$|\dot{u}(f, r)| = 2\pi f |F(f)G(f, r)|, \tag{1}$$

where G is the Fourier transform of the displacement Green's function and F is the Fourier transform of the source time function. Throughout this paper, we use a Gaussian source time function with amplitude $10^6\,\mathrm{m\,s^{-2}}$ but this is not important since we only consider small seismic perturbations (Komatitsch & Vilotte 1998) that can thus be scaled to fit any source-time function in post-processing. From Tsai & Atiganyanun (2014), considering the first N Rayleigh-wave overtones, the Green's function amplitude $|G|$ can be expressed in the far-field and for a vertical force as

$$|G(f, r)| = \sum_{i=0,N} \frac{N_i^{\mathrm{R}} k_i}{8\rho_s v_{c,i} v_{u,i}} \sqrt{\frac{2}{\pi k_i r}} e^{-\frac{\pi f r}{v_{u,i} Q_{\mathrm{R}}}}, \tag{2}$$

where the subscript $i = 0, N$ corresponds to the mode number with 0 being the fundamental mode, N^{R} is the non-dimensional Rayleigh-wave amplitude such that $N^{\mathrm{R}} = \frac{\rho(0)e_2(0)e_2(0)}{kI_1^{\mathrm{R}}}$ with $I_1^{\mathrm{R}} = \frac{1}{2}\int_0^{\infty} \rho(z)(e_1(z)^2 + e_2(z)^2)\mathrm{d}z$, ($e_1$, e_2) the horizontal and vertical Rayleigh-wave displacement eigenfunctions, $\rho(z)$ ($\mathrm{kg\,m^{-3}}$) the solid medium density at depth z, $k = \frac{2\pi f}{v_c}$ ($1\,\mathrm{m^{-1}}$) the angular wavenumber, v_c ($\mathrm{m\,s^{-1}}$) the Rayleigh-wave phase velocity, v_u ($\mathrm{m\,s^{-1}}$) the group velocity and Q_{R} the dimensionless Rayleigh-wave temporal quality factor. Attenuation is included in eq. (2) by introducing the decaying exponential by simplifying Green's functions using the asymptotic approximation to the travelling Legendre functions similar to eq. (11.23) in ch. 11 of Dahlen & Tromp (1998). Note that in this paper, we will only consider low-loss media such that $Q_{\mathrm{R}} \gtrsim 10$ (Macdonald 1959), these values being characteristic of most realistic soil conditions (Lai & Rix 2002). Finally, since the signal has finite energy, we can compute its energy spectral density (ESD) E_v ($(\mathrm{m\,s^{-1}\,Hz^{-1}})^2$), which is commonly used to measure the strength of transient signals, similar to how power spectral density is used for stationary seismic noise (Bormann 2012, ch. 4):

$$E_v(f, r) = |\dot{u}(f, r)|^2. \tag{3}$$

All ESDs are reported in decibels (dB) relative to E_v (i.e. we report $10\log_{10}E_v$). The energy distribution can provide information about the underlying physical processes: to estimate grain size of bed load (Tsai *et al.* 2012), to determine the properties of landslides (Hibert *et al.* 2017), to identify the seismic signature of debris flows (Lai *et al.* 2018), to characterize crack formation in granular materials (Michlmayr *et al.* 2012) and to study the ambient noise through cross-correlation (Zhan & Ni 2010). To build the Green's functions from eq. (2), we compute Rayleigh-wave eigenfunctions, phase and group velocities iteratively over a given frequency range following the numerical integration described, for example, in Aki & Richards (1980; ch. 7.2.1). As mentioned in the introduction, this numerical integration makes the Green's functions solution not purely analytic for an arbitrary velocity structure but for simplicity we will refer to this solution as analytic in the rest of the paper. Alternatively, instead of performing a numerical integration for each seismic model, it is also possible to derive approximations for the Rayleigh-wave eigenfunctions and velocities from non-dimensional parameters given for piecewise power-law models (Tsai & Atiganyanun 2014). These parameters enable one to only perform the computation of eigenfunctions once (for a reference power-law model and a given Poisson's ratio) to compute the Green's functions and thus help to greatly reduce the computational time and simplify the comparisons of energy distribution for various seismic models. Details about the computation of non-dimensional parameters are described in Appendix A.

To study the accuracy of the Green's function approximation, we will focus on three quantities that give us insight about the subsurface velocity and the source mechanism: the main frequency peak (or characteristic frequency) of the surface-wave energy distribution, its amplitude and its envelope. The main frequency peak and ESD amplitude carry information about the source duration and strength and the ESD envelope is strongly connected to attenuation through the exponential dependence in eq. (2). In the next sections, to illustrate the results we will show comparisons between ESDs and Fourier amplitudes as a function of distance to the source as computed with the analytic Green's functions and the fully numerical method deconvolved from the source term.

3 NUMERICAL METHOD FOR GENERATING REFERENCE SOLUTIONS

To compute a reference solution and provide meaningful comparisons with the theoretical model of Section 2, we compute high-order numerical solutions. The numerical method employed in this paper is the axisymmetric version of the seismic wave propagation package SPECFEM (Komatitsch & Vilotte 1998), which is based on a weak Galerkin formulation with spectral finite elements and Gauss–Lobatto–Legendre points. SPECFEM accounts for complex velocity structures and a constant quality factor over a specified frequency range. Note that the implementation of a constant quality factor is not straightforward in time-domain simulations (Blanc *et al.* 2016). To model viscoelastic attenuation, SPECFEM relies on a Zener solid approach based on memory variables with specific relaxation times (Carcione *et al.* 1988) that are computed through nonlinear optimization (Blanc *et al.* 2016). To obtain constant shear and compressional quality factors, Q_s and Q_p, we optimize the relaxation times over our frequency range of interest ($f = [1, 500]$ Hz) and consider five Zener solids.

4 SURFACE-WAVE AMPLITUDES WITHIN VARIOUS VELOCITY STRUCTURES

To provide the most general assessment of analytic Green's functions performance in modelling surface waves, we will focus on both elastic and viscoelastic media with increasing complexity in

Table 1. Simulation parameters for the simulation of seismic waves in a homogeneous model. L_x and L_z are the horizontal and vertical domain size, ρ is the solid density, α is the shear velocity power-law coefficient, Q_s and Q_p are the shear and compressional quality factors and f_0 is the dominant frequency.

$L_x \times L_z$ (m)	ρ (kg m^{-3})	α	Q_s	Q_p	f_0 (Hz)
1500×100	1500	0	20	40	25

shear velocity structure. Note that we only consider laterally homogeneous media, as lateral heterogeneities introduce other difficulties (reflections, mode conversions and surface to body-waves conversions) beyond the scope of this paper. Throughout the section, we use a Poisson's ratio of $\nu = 0.25$ for which Rayleigh waves are expected to dominate the vertical component of the energy distribution (Rayleigh waves being responsible for at least 70 per cent of the vertical motion, Weaver 1985). Moreover, while the semi-analytic method is valid for any given frequency, we use different frequency ranges between the pure power-law and the more realistic velocity models. This is solely to emphasize on the frequency range where the energy spectrum is impacted by discontinuities and/or strong gradients that vary between each velocity model.

Finally, in this section, although we show comparisons for a given seismic model v_s, results can be adapted to new models $\tilde{v}_s$ by considering scaled velocities such that $\tilde{v}_s(z') = v_s(z)$ with $z' = Az$. In this configuration, we obtain a very simple relationship between phase velocities $v_{c,i}(f) = \tilde{v_{c,i}}(Af)$, where $\tilde{v_{c,i}}$ corresponds to the new model velocity $\tilde{v}_s$. Finally, the updated Green's function $\tilde{G}$ using $\tilde{v}_s$ and defined in eq. (2) reads

$$\mathrm{rcl}|\tilde{G}(f/A, r)| = \frac{1}{A}|G(f, r/A)|. \tag{4}$$

4.1 Homogeneous viscoelastic model

In the case of homogeneous media, the numerical method and the approximation eq. (2) should give almost identical solutions since the surface-wave train will only be composed of the fundamental mode and will not be impacted by higher mode surface waves. The simulation parameters for this model are given in Table 1. Note that it is often assumed that $Q_R \approx Q_s$, where Q_s is the shear-wave quality factor, which is a valid assumption when considering spatially homogeneous body-wave quality factors and low shear to compressional velocity ratios such that $\frac{v_s}{v_p} \leq 0.55$, where v_p and v_s are the compressional and shear velocities, respectively. More generally, for a homogeneous medium and spatially constant quality factors and $\frac{v_s}{v_p} > 0.55$, one has to take into account the compressional quality factor Q_p. For a homogeneous seismic model and any Poisson's ratio, the Rayleigh-wave quality factor is (Macdonald 1959)

$$\frac{1}{Q_R} = (1 - m)\frac{1}{Q_s} + m\frac{1}{Q_p}, \tag{5}$$

where m is defined by

$$m = \frac{a(2-b)(1-b)}{a(2-b)(1-b) - b(1-a)(2-3b)}, \tag{6}$$

with $a = (\frac{v_c}{v_p})^2$ and $b = (\frac{v_c}{v_s})^2$. Moreover, to correctly model the energy distribution with Green's functions, one needs to properly account for the impact of attenuation on velocity dispersion, i.e the frequency dependence of the phase velocity due to visoelastic processes. Details can be found in Appendix B, where we show the impact of attenuation-induced velocity dispersion on wave propagation.

In Figs 1(a), (b) and (c), we show the time-series of vertical velocity at various distances from the source $r = 642$, 832, 895 m and their corresponding frequency-domain ESDs in Figs 1(d), (e) and (f). As expected, we observe that the signal is almost entirely composed of fundamental-mode Rayleigh waves whose main frequency shifts towards lower frequencies as distance increases because of attenuation.

In this simple case, the analytic and the numerical ESDs are in reasonable agreement throughout the spectrum, especially around the main frequency peak. In Fig. 1(g), we note that the analytic model captures well the amplitude decay with distance, for various frequencies ($f = 45, 50, 55$ Hz), owing to both geometrical spreading as $\frac{1}{\sqrt{r}}$ and attenuation as $e^{-\frac{\pi f r}{Q_R v_u}}$.

4.2 Power-law structure

The homogeneous case presented in Section 4.1 is only meaningful for validation purposes because it is not a realistic approximation for the majority of subsurface seismic models. In this section, we focus on more complex shear-velocity structures by considering 1-D power-law profiles, typical of sedimentary basins, and sometimes assumed when inverting for near-surface shear velocity (Ferrazzini *et al.* 1991; Métaxian *et al.* 1997). In this case, the shear velocity can be expressed as

$$\mathrm{rcl}v_s = v_{s,z_0}\left(\frac{z}{z_0}\right)^{\alpha}, \quad (7)$$

where z (m) is the depth, α is the power-law exponent and v_{s,z_0} (m s^{-1}) is the velocity at depth z_0 (m). To ensure numerical stability, we have to truncate the shear velocity profile near the surface in order to always have strictly positive shear velocities. We thus consider the shear velocity to be constant for depth $z < z_t$, where $z_t = 0.01$ m. Note that we verified numerically in the Supporting Information (section 1) that the error corresponding to this truncation depth z_t and resolution is negligible for the frequency range considered. In this paper, we will consider various values of α, in order to study the influence of the shear-velocity gradient with depth on wave propagation. In addition, we set $v_{s,z_0} = 2206$ m s^{-1} and $z_0 =$ 1000 m for all simulations. The density and velocity profiles are given in Table 2 and taken from Boore & Joyner (1997) for a typical sedimentary basin.

4.2.1 *Elastic power-law medium*

Before introducing viscoelasticity, we study a purely elastic medium with a power-law shear velocity structure. By ignoring attenuation, we avoid issues related to physical dispersion presented in the last section. Also, in the elastic case, the computation of Green's functions is straightforward and enables us to focus only on the impact of the power-law profile on the time-series and ESDs.

We run a simulation with the parameters presented in Table 2 labelled as Elastic. Fig. 2 shows the vertical velocity time-series and corresponding ESDs at three different distances. In the left-hand panels (a), (b) and (c), we note that the subsurface velocity variations lead to a more complex waveform with multiple arrivals and highly dispersive surface waves. In panels (d), (e) and (f), we observe that the analytic model with the fundamental mode only captures well the amplitude and shape of the energy distribution. Nonetheless, we note that higher mode (which propagates at a larger velocity than the fundamental mode) arrivals introduce oscillations in the ESD that can be captured by considering the first higher order mode along with the fundamental mode.

Fig. 2(g) shows comparisons of spectral amplitudes for the theoretical model (the dashed lines) and the Fourier transform of the numerical solutions (the solid lines) against distance from the source for various frequencies ($f = 35, 40, 50$ Hz) for which surface waves are dominant. The amplitudes are well captured by the analytic Green's functions with an error of < 5 per cent for all distances. We also observe that the amplitude decay with distance, as a result of geometrical attenuation, is accurately reproduced by the theoretical model that is expected when there is no lateral variation in velocity structure. The good agreement of amplitude and peak frequency shows that the fundamental mode provides an accurate description of wave propagation for low frequencies $f < 50$ Hz and this velocity profile and that higher mode Rayleigh waves do not play a significant role in the energy distribution.

4.2.2 *Viscoelastic power-law medium*

The absence of attenuation in the previous simulation is not a realistic approximation since relaxation processes strongly alter the shape, amplitude and frequency peak of the energy distribution. To study the influence of viscoelasticity on surface-wave propagation in a complex velocity structure, we consider quality factors typical of unconsolidated sedimentary basins. These Q values combined with a power-law shear velocity profile are a good approximation of near-surface seismic structures (Anderson & Hough 1984). For models with varying body-wave quality factors that vary with depth, the Rayleigh-wave quality factor is frequency dependent and depends on the shear and compressional velocities (Anderson *et al.* 1965). Equations are presented in the Supporting Information (section 2), along with a figure showing the frequency dependence of the Rayleigh-wave quality factor for a realistic 1-D velocity profile extracted from the SCEC model. We run a simulation with the parameters given in Table 2 labelled as 'Viscoelastic I'.

The comparisons of time-series and ESDs for both the numerical simulations and the analytic model at various distances from the source are presented in Fig. 3. The amplitude and the shape of the ESDs are well captured by the fundamental-mode theoretical model. Again, by adding in the first higher mode Rayleigh wave one is able to reproduce the oscillatory behaviour of the ESDs. In Fig. 3(g), we also compare the vertical velocity response against distance for various frequencies ($f = 10, 15, 20$ Hz) for which the surface-wave energy is still dominant. The velocity amplitude decay with distance is well captured by the analytic model for low frequencies with an error < 10 per cent. The introduction of attenuation leads to a slightly more intricate surface energy distribution than for an elastic media over the same frequency range. First, the main ESD frequency peak shifts towards lower frequencies as the surface waves propagate in this dissipative medium. Second, we observe, as previously mentioned, that arrivals from the various Rayleigh-wave modes introduce periodicity in the time-series and, therefore, additional harmonics in the frequency domain as in the elastic case. Finally, while most of the ESD consists of the first two modes, we note that the theoretical model seems not to fully capture the variations of the ESD for frequencies above a certain threshold f_0 that varies with distance (e.g. $f > 35$ Hz in Fig. 3f). The frequency

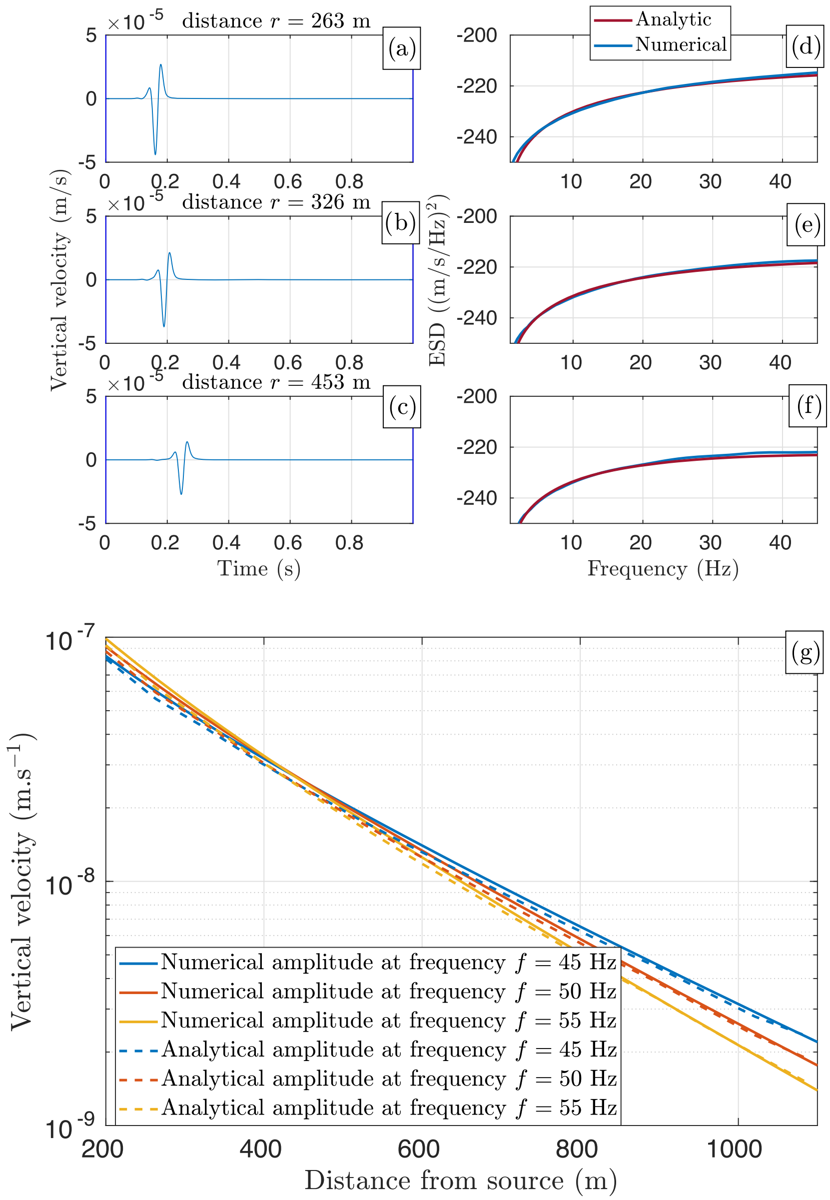

Figure 1. Panels (a), (b) and (c), vertical velocity perturbations against time, for the simulation parameters presented in Table 1, at various distances from the source, respectively, from top to bottom, $r = 263, 326, 453$ m. Panels (d), (e) and (f), the corresponding energy spectral density against frequency computed from the numerical simulation (blue) and the fundamental-mode analytic model (red). Panel (g), vertical velocity against distance of numerical simulations (the solid lines) and theoretical model (the dashed lines) at frequency $f = 45$ Hz (blue), $f = 50$ Hz (red), $f = 55$ Hz (yellow).

Table 2. Simulation parameters for the simulation of seismic waves in both an elastic (Elastic) and viscoelastic models (Viscoelastic I and Viscoelastic II) with a shear velocity power-law structure. L_x and L_z are the horizontal and vertical domain sizes, respectively, ρ is the solid density, α is the shear velocity power-law coefficient, Q_s and Q_p are the shear and compressional quality factors, respectively, and f_0 is the dominant frequency. The double apostrophe ” means that the value is unchanged from the previous line.

	$L_x \times L_z$ (m)	ρ (kg m^{-3})	α	Q_s	Q_p	f_0 (Hz)
Elastic	1500×600	1500	0.272	9999	9999	25
Viscoelastic I	”	”	”	20	40	”
Viscoelastic II	”	”	0.1	20	40	”
Viscoelastic III	”	”	0.45	”	”	”

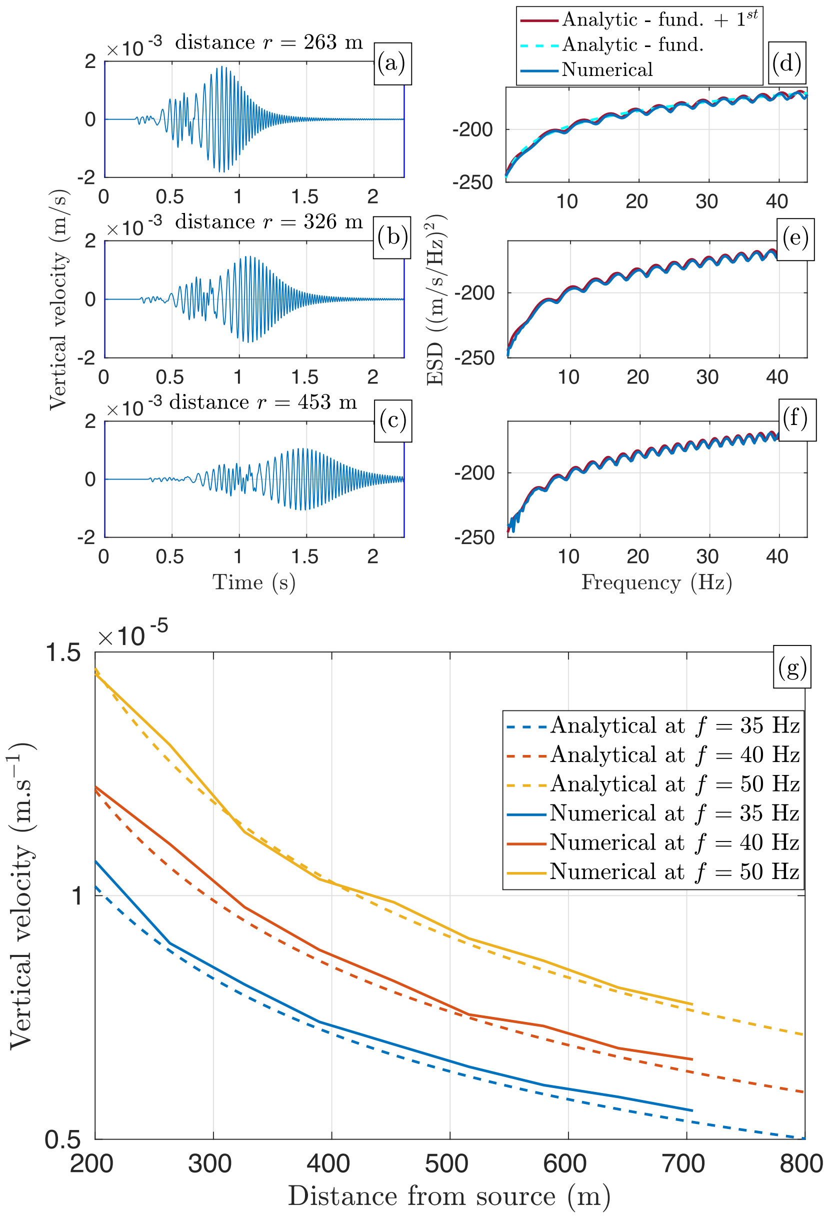

Figure 2. Panels (a), (b) and (c), vertical velocity perturbations against time, for the simulation parameters 'Elastic' presented in Table 2, at various distances from the source, respectively, from top to bottom, $r = 263$, 326, 453 m. Panels (d), (e) and (f), the corresponding energy spectral density against frequency computed from the numerical simulation (blue), the fundamental + first-mode analytic model (red) and the fundamental-mode analytic model (dashed blue). Panel (g), comparisons of the Fourier transforms of the vertical velocity against distance from the simulations (solid) and the theoretical model (dashed) at various frequency $f = 35$ Hz (blue), $f = 45$ Hz (orange) and $f = 50$ Hz (yellow). Panel (g), comparisons of the Fourier transforms of the vertical velocity against distance from the simulations (solid) and the theoretical model (dashed) at various frequency $f = 35$ Hz (blue), $f = 45$ Hz (orange) and $f = 50$ Hz (yellow). Note that results can be scaled for any new shear-velocity model $\tilde{v}_s(Az) = v_s(z)$, where A is a scalar and z is the depth, using eq. (4).

threshold corresponds to the transition where the higher order modes begin to be significant over the first two modes.

The energy amplitude of the higher order modes is dependent on the subsurface velocity model, as larger velocity gradients lead to more trapped energy near the surface. The power α defined in eq. (7) plays a key role in how much energy is trapped near the surface and, therefore, also strongly affects the overall energy distribution. With lower values of α, the shear-wave velocity gradient with depth will also decrease, and consequently the energy of waves trapped at the surface will be smaller. With larger values of α, higher mode energy grows and the energy of the fundamental-mode surface wave will be less and less dominant. To illustrate this point, we compare the previous simulation ($\alpha = 0.272$) with simulations with $\alpha = 0.1$ and $\alpha = 0.45$ together with the parameters from Table 2, respectively, labelled as 'Viscoelastic II' and 'Viscoelastic III'.

Results are shown in Fig. 4, for $\alpha = 0.1$ panels (a) and (c) and for $\alpha = 0.45$ panels (b) and (d). We observe in panels (a) and (c) that the ESD is largely dominated by the fundamental mode as the velocity gradients are small. Conversely, in panels (b) and (d), we note that due to the large shear-velocity gradient with depth, the high-frequency part (for $f > 15$ Hz) of the spectrum is highly

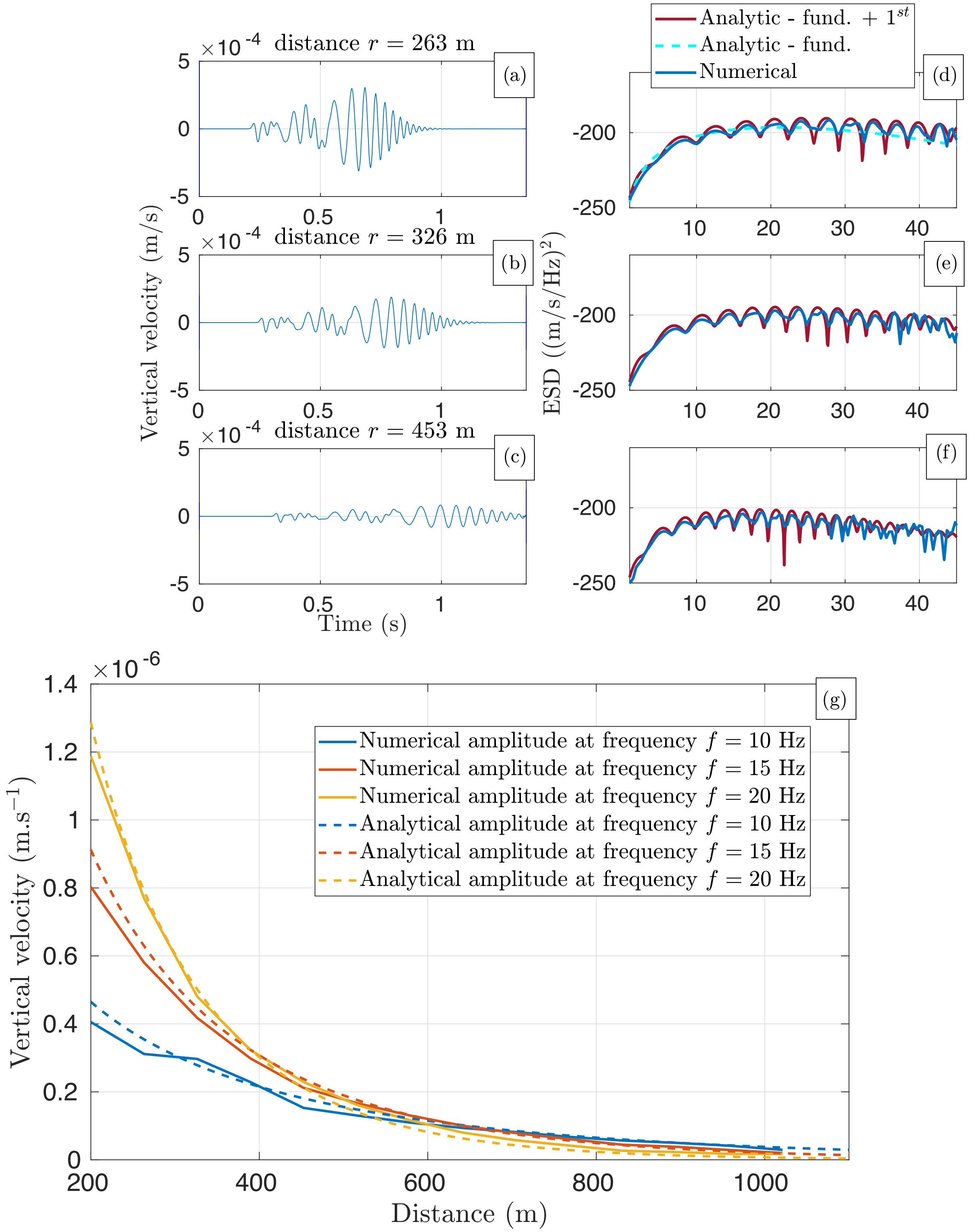

Figure 3. Panels (a), (b) and (c), vertical velocity perturbations against time, for the simulation parameters 'Viscoelastic I' presented in Table 2 at various distances from the source, respectively, from top to bottom, $r = 263, 326, 453$ m. Panels (d), (e) and (f), the corresponding energy spectral density against frequency computed from the numerical simulation (blue), the fundamental + first-mode analytic model (red) and the fundamental-mode analytic model (dashed blue). Panel (g), Spectral vertical velocity against distance from the source, for the simulation parameters 'Viscoelastic I' presented in Table 2, from numerical simulations (the solid lines) and analytic Green's functions (the dashed lines) for various frequencies $f = 10$ Hz (blue), $f = 15$ Hz (orange) and $f = 20$ Hz (yellow). Note that results can be scaled for any new shear-velocity model $\tilde{v}_s(Az) = v_s(z)$, where A is a scalar and z is the depth, using eq. (4).

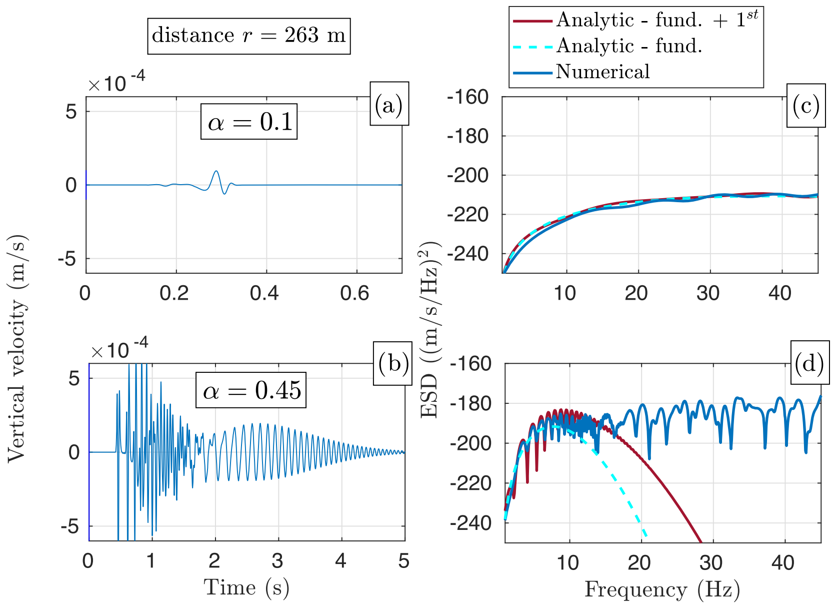

Figure 4. Panels (a) and (b), vertical velocity perturbations against time, for the simulation parameters 'Viscoelastic II' presented in Table 2 (panel a) and 'Viscoelastic III' presented in Table 2 (panel b) at $r = 263$ m from the source. Panels (c) and (d), the corresponding energy spectral density against frequency computed from the numerical simulation (blue), the fundamental + first-mode analytic model (red) and the fundamental-mode analytic model (dashed blue). Note that results can be scaled for any new shear-velocity model $\tilde{v}_s(Az) = v_s(z)$, where A is a scalar and z is the depth, using eq. (4).

impacted by higher modes. By running frequency-domain simulations using Computer Program in Seismology (Herrmann 2013), we identify that those higher mode arrivals correspond to modes larger than the fifth mode. Moreover, at low frequency and for a large α value the fundamental mode does not fully capture velocity amplitude and we have to include the first overtone to properly reproduce the energy distribution. For such large values of α, the hypothesis that surface-wave energy dominates the spectrum should be tempered as pointed out from observations by Bonnefoy-Claudet *et al.* (2006). In Fig. A2, we plot the Green's function amplitude against α and we observe that for $\alpha \approx 0.5$, the first higher order and fundamental-mode Rayleigh wave Green's functions have comparable amplitudes. Nonetheless, the semi-analytic approach provides a reasonable ESD estimate using the first fundamental and first overtone only at low frequencies.

To provide a rough empirical estimate of the frequency threshold f_0, where modes beyond the first two need to be accounted for to accurately model ESD amplitudes, we ran simulations with the same Poisson's ratio and various $\alpha < 0.5$, values for typical sedimentary basins (Plumier & Doneux 2003; Chandler *et al.* 2005, 2006; Huang *et al.* 2007; Wang & Wang 2016). We were able to approximate f_0 as $f_0 \approx \frac{1}{2\alpha} f_0^r(Q_R)$, where $f_0^r(Q_R)$ is the quality-factor dependent surface-wave peak frequency at distance r from the source. For a given constant quality factor, f_0^r can be derived analytically from the non-dimensional parameters and is given in eq. (A7). With increasing α, $f_0 \to 0$ and we can expect higher modes to play a significant role in the low-frequency energy distribution. More details about this empirical estimate are given in Appendix C.

4.3 Realistic basins

The comparisons described in Section 4 are only based on pure power-law near-surface velocity structures, while real seismic models are often more discontinuous. To analyse more realistic velocity models, we now consider a generic rock site velocity profile from Boore & Joyner (1997), which is composed of piecewise power-law scalings as well as discontinuous 1-D models extracted from the SCEC Community Velocity Model for Southern California model version 4.26 (CVM-S4.26, Lee *et al.* 2014).

4.3.1 Piecewise power-law model

Before focusing on viscoelastic structures from the SCEC model, we extend last section's study of a simple power-law velocity model to a piecewise power-law model. In this case, the single power-law approximation of the ESD is no longer valid but, as suggested in Tsai & Atiganyanun (2014), the frequency transition between each power-law scaling tends to occur when phase velocities cross. This frequency roughly corresponds to the expected depth sensitivity of Rayleigh waves for a given frequency. To compare the analytic and the numerical approach, we use the velocity model from Boore & Joyner (1997) composed of five separate piecewise power-law scalings as

$$v_s(z) = \begin{cases} 245, & z \le 1, \\ 2206\left(\frac{z}{z_0}\right)^{0.272}, & 1 < z \le 30 \\ 3542\left(\frac{z}{z_0}\right)^{0.407}, & 30 < z \le 190 \\ 2505\left(\frac{z}{z_0}\right)^{0.199}, & 190 < z \le 4000 \\ 2927\left(\frac{z}{z_0}\right)^{0.086}, & 4000 < z \end{cases}. \tag{8}$$

Shear- and compressional-wave velocities, phase velocities and quality factors are shown in Fig. 5. We observe in panel (c) that the transitions between the power-law scalings $\alpha = 0.199$ and $\alpha = 0.272$ occur around $f \approx 2.$ Hz and $\alpha = 0.407$ and the transition between $\alpha = 0.407$ is around $f \approx 6.3$ Hz. Together with the velocity model of eq. (8), we consider a realistic attenuation model of Graves' (Graves & Pitarka 2010) presented in Fig. 5(b). We show the waveform and ESD comparisons in Fig. 6. In panels (a), (b) and (c), we observe

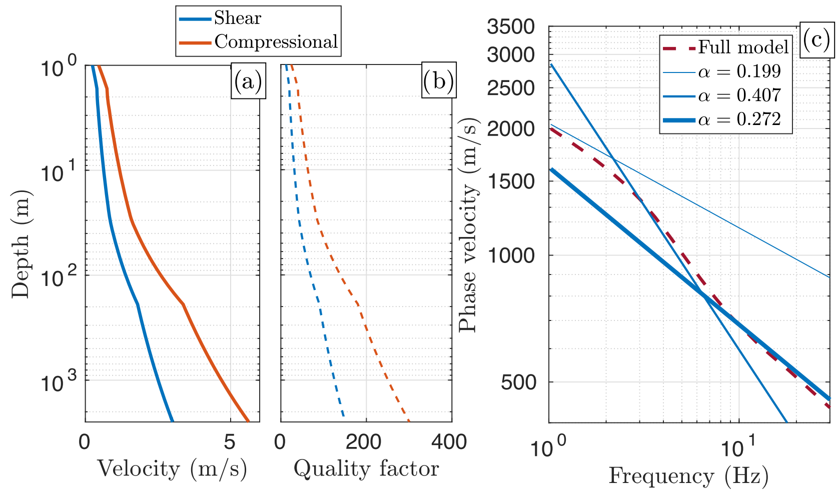

Figure 5. Panel (a), Shear (blue) and compressional (orange) velocity profile against depth for Boore's model. Panel (b), corresponding Shear (blue) and compressional (orange) quality factors against depth for the low-frequency Graves attenuation model. Panel (c), Rayleigh-wave phase velocities against frequency for the true seismic model 'True model' (the dashed red line) and the three piecewise velocity models with $\alpha = 0.272$ (the thick blue line), $\alpha = 0.407$ (the blue line) and $\alpha = 0.199$ (the thin blue line).

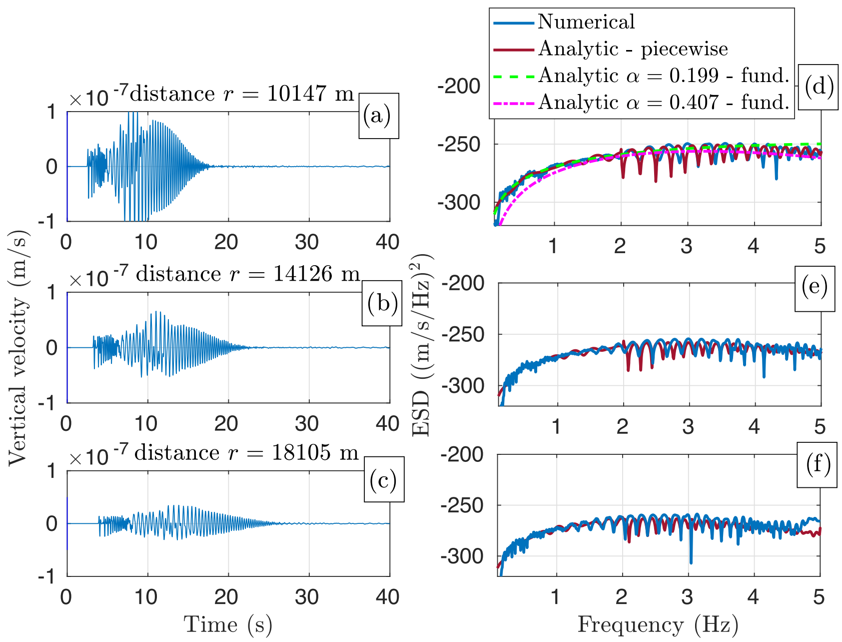

Figure 6. Panels (a), (b) and (c), vertical velocity perturbations against time, for the piecewise power-law model from Boore at various distances from the source, respectively, from top to bottom, $r = 10.1$, 14.1, 18.1 km. Panels (d), (e) and (f), energy spectral density against frequency for the same simulation parameters computed from the numerical simulation (blue) the piecewise analytic model (red), the analytic model with the power-law scaling $\alpha = 0.199$ (dashed green) and the power-law scaling $\alpha = 0.407$ (dashed pink).

numerous highly dispersive higher mode Rayleigh waves that translate into a complex energy distribution. In panels (d), (e) and (f), we note that for $f < 2$ Hz the numerical ESD is very well captured by the power-law scaling $\alpha = 0.199$ and for $5 > f \geq 2$ Hz, the power-law scaling $\alpha = 0.407$ provides the best fit. We also observe that for $5 > f \geq 2$ Hz, higher modes play a more important role than for $f < 2$ Hz translating into larger spectrum oscillations that are captured by the non-dimensional piecewise model. We conclude that the Rayleigh-wave ESD from the piecewise velocity model defined in eq. (8) can be very well reproduced by simply considering various non-dimensional power-law scalings described in Appendix A over the right frequency ranges.

4.3.2 *Los Angeles Basin—highly discontinuous shear-velocity model*

The near-surface velocity model presented in Fig. 5(a) does not have strong discontinuities. However, in certain basins, the velocity profile can be more discontinuous because of the presence of other shallow low-velocity sedimentary layers (Benjumea *et al.* 2016) or,

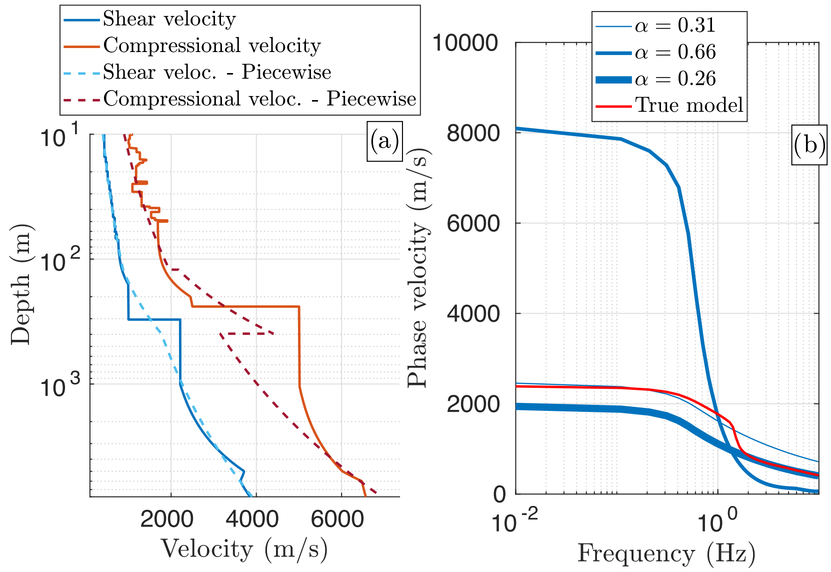

Figure 7. Panel (a), Shear (blue) and compressional (orange) velocity profile against depth (log scale) for the Pasadena area and corresponding velocity piecewise model from eq. (9) (dashed). Panel (b), fund-mode Rayleigh-wave phase velocities against frequency for the true seismic model 'True model' (the red line) and the three piecewise velocity models with $\alpha = 0.31$ (the thin blue line), $\alpha = 0.66$ (the blue line) and $\alpha = 0.26$ (the thick blue line).

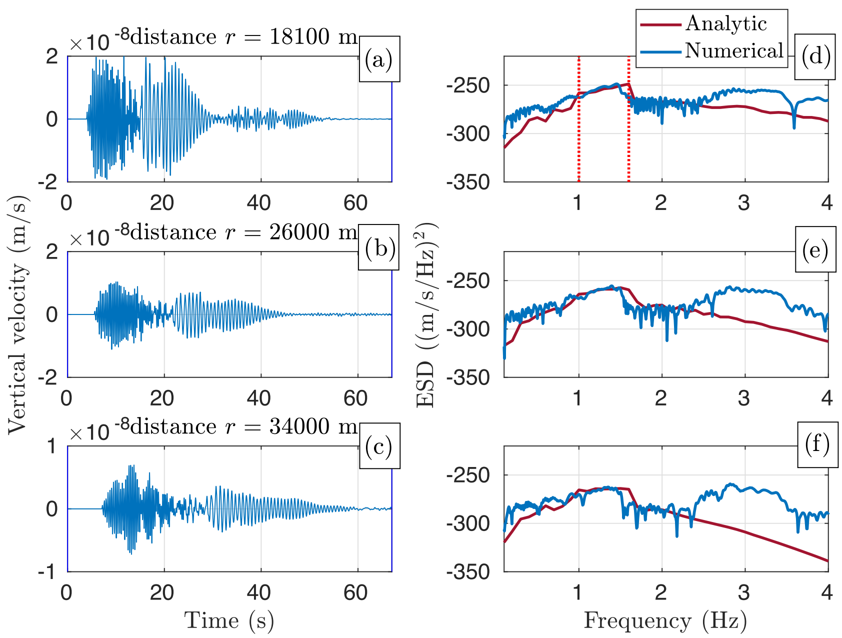

Figure 8. Panels (a), (b) and (c), vertical velocity perturbations against time, for the Los Angeles Basin model, at various distances from the source, respectively, from top to bottom, $r = 18.1$, 26, 34 km. Panels (d), (e) and (f), corresponding energy spectral density against frequency for the same simulation parameters computed from the numerical simulation (the blue line) and the analytic model with the fundamental-mode and first overtone Rayleigh wave (the dashed red line). In Panel (d), we also show the analytic power-law ESDs against frequency for the various scalings $\alpha = 0.315$ (the thin red line), $\alpha = 0.71$ (the red line) and $\alpha = 0.263$ (the thick red line). The dashed red vertical lines correspond to the frequency bounds between each power-law scalings.

at larger depths, owing to the rock-sediment boundary. As in the previous section, the power-law approximation is no longer valid but one can try to approximate a generic shear-velocity profile as a combination of piecewise power-law velocity structures. In this section, we will study the impact of a strong shear-wave velocity discontinuity on the energy distribution and explore the possibility of predicting the ESD through piecewise power-law scalings.

To assess the accuracy of Green's functions for non-power-law structures, we consider another velocity profile, shown in Fig. 7, at latitude 34.12 and longitude −118.12, corresponding to the Pasadena area in Los Angeles county extracted from the SCEC 4.26 model. The Pasadena profile shows a strong discontinuity around $z = 300$ m that will impact low-frequency surface-wave eigenfunctions.

In order to use simple power-law scalings to predict the ESD, we have to first discretize the velocity model. Most of the velocity structure can be very well described by several joined power-law scalings. However, a discontinuity cannot be fully captured by a power law and needs to be crudely approximated. This velocity jump can be roughly reproduced by large α and velocity v_{s,z_0} values in eq. (7), which will lead to a very steep velocity profile with depth. Therefore, to discretize the velocity profile showed in Fig. 7, we pick two depths $z_1 = 190$ m and $z_2 = 600$ m and define three piecewise power-law scalings such that

$$\begin{aligned} &1700(\tfrac{z}{z_0})^{0.31}, && z \leq z_1, \\ &3673(\tfrac{z}{z_0})^{0.66}, && z_1 < z \leq z_2, \\ &2240(\tfrac{z}{z_0})^{0.26}, && z_2 < z, \end{aligned} \tag{9}$$

where we choose the power-law scalings by finding the best shear-wave velocity fitting of the true velocity model over the various depth ranges. Along with the shear-velocity model, we have to provide the compressional velocity model and the density model. To compute the compressional velocities, we will use a constant Poisson's ratio over each interval defined in eq. (9). As the Poisson's ratio varies with depth, we calculate the geometric mean of the Poisson's ratio from the SCEC model over each interval. Similarly, we compute the density model by taking the geometric mean of the density from the SCEC model over each interval. In Fig. 7(a), we show the true and power-law shear-velocity structures. Considering the discontinuous profile in eq. (9), we can compute the corresponding phase velocities using the scalings presented in Appendix A. Similar to the previous model, we define the frequency transition between each power-law scaling by determining where the phase velocities cross for each mode. As mentioned in Section 4.2, when $\alpha > 0.5$, the first overtone will dominate over the fundamental mode and, therefore, we will consider the first two modes to compute the analytical ESD. In Fig. 7(b), we show the fundamental-mode Rayleigh-wave phase velocities for the true seismic model and the various power-law scalings. The various phase velocities cross around $f \approx 1$ Hz and $f \approx 1.55$ Hz, at which the first higher order mode wavenumbers are, respectively, $1/k \approx 100$ m and $1/k \approx 300$ m close to depth of the discontinuity. We observe that the power-law scalings roughly approximate the variations of the true phase-velocity model over their own frequency range.

For the highly discontinuous velocity model, we show the numerical time-series in Figs 8(a), (b) and (c). We observe that the presence of a shallow discontinuity leads to a highly dispersive fundamental-mode Rayleigh wave and the propagation of a high-amplitude first-overtone Rayleigh wave. This is expected in discontinuous media such as shallow sedimentary basins (Bonnefoy-Claudet *et al.* 2006; Rivet *et al.* 2015). In panels (d), (e) and (f), we observe a frequency peak around $f \approx 1.3$ Hz corresponding to the high-amplitude first higher order mode Rayleigh wave and, at higher frequencies, another peak around $f \approx 3$ Hz owing to higher mode Rayleigh waves.

In Figs 8(d), (e) and (f), we show the ESDs built from the piecewise power-law scalings of eq. (9) for the fundamental and first Rayleigh-wave modes. We observe that by simply considering the first overtone $N = 1$ along with the fundamental mode, we obtain a good fit at low frequencies between the numerical and the analytic Green's functions. However, around the frequency bounds denoted by the dashed vertical lines, we observe discrepancies in amplitude in the transition zones between each piecewise power-law scalings because of the rough approximation of the solutions. Indeed, power-law scalings lead to constant non-dimensional amplitudes N^{R} (Tsai & Atiganyanun 2014) that cannot fully capture the amplitude variations of the true seismic model. Finally, around $f \approx 3$ Hz, we observe that a second energy peak is not captured by the analytical ESD. This secondary peak is due to higher modes surface waves that dominate over the first two modes in the $f = [2.5, 4]$ Hz frequency range.

5 CONCLUSIONS

In this paper, we investigated the capability of a fast semi-analytic method to compute Rayleigh-wave energy spectra within elastic and viscoelastic media with increasing shear-wave model complexity. The method is based on the non-dimensionalization of the Rayleigh-wave governing equations and provides an exact expression for the phase and group velocities as well as the Green's functions in pure 1-D shear-wave power-law velocity models. We compared energy distribution predictions from surface-wave Green's functions to high-order numerical solutions for an impulsive source. The semi-analytic ESD captures well the main frequency peak and the amplitude of the ESDs of the fundamental-mode Rayleigh wave in both elastic and viscoelastic power-law structures. The reasonable agreement between ESDs shows that the body-to-surface-wave conversions and higher Rayleigh-wave modes do not have a strong impact on the energy distribution in smoothly varying shear-velocity structures. Attenuation plays an important role in the energy distribution and the computation of the Rayleigh-wave quality factor and its frequency dependence requires special attention when considering highly heterogeneous body-wave quality factors. Especially for very low Q values, viscoelastic-induced velocity dispersion should be carefully taken into account as it leads to a substantial change in the phase and group velocities. At short distances from the source, and for large shear-velocity depth gradients or low attenuation, the low-frequency spectral response can be dominated by very high mode surface waves that can be described by the power-law scalings. More precisely, for a shear-wave power-law structure, we derived an empirical frequency range where body-wave energy is dominant $f > \frac{1}{2\alpha} f_0^r(Q_{\mathrm{R}})$, where $f_0^r(Q_{\mathrm{R}})$ is the quality-factor dependent fundamental-mode surface-wave peak frequency at a distance r, for a quality factor Q_{R} from the source and α is the power defining the shear velocity profile. Also, for large values $\alpha > 0.5$, the first higher order mode Rayleigh waves will start to dominate the energy spectrum and cannot be neglected anymore. Semi-analytic non-dimensional Green's functions can also provide an estimate of the ESD for realistic 1-D shear velocity structures and complex attenuation models. For velocity structures that are close to a piecewise power-law model, the semi-analytic approach can describe the ESD using the first fundamental and first overtone only. The frequency range of validity for each power-law scaling can be derived from their phase velocities corresponding roughly to the depth sensitivity of Rayleigh waves. Finally, highly discontinuous models can also be approximated by a combination of power-law scalings. They provide a good estimate of the amplitude and variations of the energy distribution although the predictions are quite poor around the frequency bounds of each power-law scaling. Future studies should focus on the assessment of the method to perform simple inversions of surface-wave energy spectra to derive velocity models or source mechanisms. Moreover, future papers should investigate the ability of power-law scaling to model the horizontal component of the energy distribution where Love waves are expected to dominate (Bonnefoy-Claudet *et al.* 2006).

ACKNOWLEDGEMENTS

The authors would like to thank the two anonymous reviewers that greatly helped improving the paper.

REFERENCES

Aki, K. & Richards, P., 1980. *Quantitative Seismology,* Vol. **II,** W.H. Freeman and Company.

Anderson, D.L., Ben-Menahem, A. & Archambeau, C.B., 1965. Attenuation of seismic energy in the upper mantle, *J. geophys. Res.,* **70**(6), 1441–1448.

Anderson, J.G. & Hough, S.E., 1984. A model for the shape of the Fourier amplitude spectrum of acceleration at high frequencies, *Bull. seism. Soc. Am.,* **74**(5), 1969–1993.

Bard, P.-Y., 1999. Microtremor measurements: a tool for site effect estimation?, eds ,Irikura, K., ,Kudo, K., ,Okada, H. & ,Sasatani, T., in *Second International Symposium on the Effects of Surface Geology on seismic motion, Yokohama,* Vol. **3,** pp. 1251–1279, Balkema.

Benjumea, B., Macau, A., Gabàs, A. & Figueras, S., 2016. Characterization of a complex near-surface structure using well logging and passive seismic measurements, *Solid Earth,* **7**(2), 685–701.

Blanc, E., Komatitsch, D., Chaljub, E., Lombard, B. & Xie, Z., 2016. Highly accurate stability-preserving optimization of the Zener viscoelastic model, with application to wave propagation in the presence of strong attenuation, *Geophys. J. Int.,* **205**(1), 427–439.

Bonnefoy-Claudet, S., Cotton, F. & Bard, P.-Y., 2006. The nature of noise wavefield and its applications for site effects studies: a literature review, *Earth-Sci. Rev.,* **79**(3–4), 205–227.

Boore, D.M. & Joyner, W.B., 1997. Site amplifications for generic rock sites, *Bull. seism. Soc. Am.,* **87**(2), 327–341.

Bormann, P., 2012. *New Manual of Seismological Observatory Practice (NMSOP-2),* Deutsches GeoForschungszentrum GFZ; IASPEI.

Burtin, A., Bollinger, L., Vergne, J., Cattin, R. & Nábělek, J., 2008. Spectral analysis of seismic noise induced by rivers: a new tool to monitor spatiotemporal changes in stream hydrodynamics, *J. geophys. Res.,* **113**(B5), doi:10.1029/2007JB005034.

Carcione, J.M., Kosloff, D. & Kosloff, R., 1988. Wave propagation simulation in a linear viscoelastic medium, *Geophys. J. Int.,* **95**(3), 597–611.

Chandler, A., Lam, N. & Tsang, H., 2005. Shear wave velocity modelling in crustal rock for seismic hazard analysis, *Soil Dyn. Earthq. Eng.,* **25**(2), 167–185.

Chandler, A., Lam, N. & Tsang, H., 2006. Regional and local factors in attenuation modelling: Hong kong case study, *J. Asian Earth Sci.,* **27**(6), 892–906.

Dahlen, F. & Tromp, J., 1998. *Theoretical Global Seismology,* Princeton University press.

Ferrazzini, V., Aki, K. & Chouet, B., 1991. Characteristics of seismic waves composing Hawaiian volcanic tremor and gas-piston events observed by a near-source array, *J. geophys. Res.,* **96**(B4), 6199–6209.

Gimbert, F., Tsai, V.C. & Lamb, M.P., 2014. A physical model for seismic noise generation by turbulent flow in rivers, *J. geophys. Res.,* **119**(10), 2209–2238.

Graves, R.W. & Pitarka, A., 2010. Broadband ground-motion simulation using a hybrid approach, *Bull. seism. Soc. Am.,* **100**(5A), 2095–2123.

Haney, M.M. & Tsai, V.C., 2017. Perturbational and nonperturbational inversion of Rayleigh-wave velocities, *Geophysics,* **82**(3), F15–F28.

Herrmann, R.B., 2013. Computer programs in seismology: an evolving tool for instruction and research, *Seismol. Res. Lett.,* **84**(6), 1081–1088.

Hibert, C., Ekström, G. & Stark, C.P., 2017. The relationship between bulk-mass momentum and short-period seismic radiation in catastrophic landslides, *J. geophys. Res.,* **122**(5), 1201–1215.

Huang, M.-W., Wang, J.-H., Ma, K.-F., Wang, C.-Y., Hung, J.-H. & Wen, K.-L., 2007. Frequency-dependent site amplifications with $f > 0.01$ Hz evaluated from velocity and density models in central Taiwan, *Bull. seism. Soc. Am.,* **97**(2), 624–637.

Knopoff, L., 1937. Green's function for eigenvalue problems and the inversion of Love wave dispersion data, *Geophys. J. Int.,* **4**(1), 161–173.

Komatitsch, D. & Vilotte, J.-P., 1998. The spectral element method: an efficient tool to simulate the seismic response of 2D and 3D geological structures, *Bull. seism. Soc. Am.,* **88**(2), 368–392.

Lai, C.G. & Rix, G.J., 2002. Solution of the Rayleigh eigenproblem in viscoelastic media, *Bull. seism. Soc. Am.,* **92**(6), 2297–2309.

Lai, V.H., Tsai, V.C., Lamb, M.P., Ulizio, T.P. & Beer, A.R., 2018. The seismic signature of debris flows: flow mechanics and early warning at Montecito, California, *Geophys. Res. Lett.,* **45**(11), doi:10.1029/2018GL077683.

Larose, E. *et al.*, 2015. Environmental seismology: what can we learn on earth surface processes with ambient noise? *J. Appl. Geophys.,* **116,** 62–74.

Lee, E.-J., Chen, P., Jordan, T.H., Maechling, P.B., Denolle, M.A. & Beroza, G.C., 2014. Full-3-D tomography for crustal structure in southern California based on the scattering-integral and the adjoint-wavefield methods, *J. geophys. Res.,* **119**(8), 6421–6451.

Liu, H.-P., Anderson, D.L. & Kanamori, H., 1976. Velocity dispersion due to anelasticity; implications for seismology and mantle composition, *Geophys. J. Int.,* **47**(1), 41–58.

Macdonald, J.R., 1959. Rayleigh-wave dissipation functions in low-loss media, *Geophys. J. Int.,* **2**(2), 132–135.

McNutt, S.R. & Nishimura, T., 2008. Volcanic tremor during eruptions: temporal characteristics, scaling and constraints on conduit size and processes, *J. Volcanol. Geotherm. Res.,* **178**(1), 10–18.

Métaxian, J.-P., Lesage, P. & Dorel, J., 1997. Permanent tremor of Masaya volcano, Nicaragua: wave field analysis and source location, *J. geophys. Res.,* **102**(B10), 22 529–22 545.

Michlmayr, G., Cohen, D. & Or, D., 2012. Sources and characteristics of acoustic emissions from mechanically stressed geologic granular media-a review, *Earth-Sci. Rev.,* **112**(3-4), 97–114.

Perron, V., Gélis, C., Froment, B., Hollender, F., Bard, P.-Y., Cultrera, G. & Cushing, E.M., 2018. Can broad-band earthquake site responses be predicted by the ambient noise spectral ratio? insight from observations at two sedimentary basins, *Geophys. J. Int.,* **215**(2), 1442–1454.

Plumier, A., Doneux, C., Camelbeeck, T., Rompay, G.V., Jongmans, D., Wathelet, M., Teerlynck, H. & Van Nguyen , F.C., 2003. Seismic risk assessment and mitigation for Belgium in the frame of eurocode 8, in *Programme of scientific support for standardisation and technical regulations,* p. 7, Belgian Science Policy

Rivet, D., Campillo, M., Sanchez-Sesma, F., Shapiro, N.M. & Singh, S.K., 2015. Identification of surface wave higher modes using a methodology based on seismic noise and coda waves, *Geophys. J. Int.,* **203**(2), 856–868.

Tomar, G., Stutzmann, E., Mordret, A., Montagner, J.-P., Singh, S.C. & Shapiro, N.M., 2018. Joint inversion of the first overtone and fundamental mode for deep imaging at the Valhall oil field using ambient noise, *Geophys. J. Int.,* **214**(1), 122–132.

Tsai, V.C. & Atiganyanun, S., 2014. Green's functions for surface waves in a generic velocity structure, *Bull. seism. Soc. Am.,* **104**(5), 2573–2578.

Tsai, V.C. & Ekström, G., 2007. Analysis of glacial earthquakes, *J. geophys. Res.,* **112**(F3), doi:10.1029/2006JF000596.

Tsai, V.C., Minchew, B., Lamb, M.P. & Ampuero, J.-P., 2012. A physical model for seismic noise generation from sediment transport in rivers, *Geophys. Res. Lett.,* **39**(2), doi:10.1029/2011GL050255.

Wang, S.-Y. & Wang, H.-Y., 2016. Site-dependent shear-wave velocity equations versus depth in California and Japan, *Soil Dyn. Earthq. Eng.,* **88,** 8–14.

Weaver, R.L., 1985. Diffuse elastic waves at a free surface, *J. acoust. Soc. Am.,* **78**(1), 131–136.

Xia, J., Miller, R.D. & Park, C.B., 1999. Estimation of near-surface shear-wave velocity by inversion of Rayleigh waves, *Geophysics,* **64**(3), 691–700.

Yanovskaya, T., Levshin, A., Its, E., Lander, A., Bukchin, B., Barmin, M. & Ratnikova, L., 2012. *Seismic Surface Waves in a Laterally Inhomogeneous Earth,* Vol. **9,** Springer Science & Business Media.

Zhan, Z. & Ni, S., 2010. Stationary phase approximation in the ambient noise method revisited, *Earthq. Sci.,* **23**(5), 425–431.

SUPPORTING INFORMATION

Supplementary data are available at *GJI* online.

supplementary_sediments_brissaud.pdf
Please note: Oxford University Press is not responsible for the content or functionality of any supporting materials supplied by the authors. Any queries (other than missing material) should be directed to the corresponding author for the paper.

APPENDIX A: NON-DIMENSIONAL PARAMETERS IN SHEAR-VELOCITY POWER-LAW STRUCTURES

In this appendix, we recall the main results of Tsai & Atiganyanun (2014) regarding the expression of the Rayleigh-wave phase velocity and amplitude in a shear-wave power-law structure. We consider a shear-velocity power-law structure v_s with a constant Poisson's ratio ν and constant density, such that

$$v_s = v_{s,z_0}\left(\frac{z}{z_0}\right)^{\alpha}, \tag{A1}$$

where v_{s,z_0} is the shear-velocity at depth z_0. Then, we express the phase velocity as

$$v_c = \frac{\omega}{k} = v_{c,0}\left(\frac{\omega}{\omega_0}\right)^{-\frac{\alpha}{1-\alpha}}, \tag{A2}$$

where $k = \frac{\omega}{v_c}$ is the wavenumber, ω_0 is the reference pulsation and $v_{c,0}$ the phase velocity at zero frequency such that

$$v_{c,0} = \epsilon_c\left(\frac{v_{s,z_0}}{(\omega_0 z_0)^{\alpha}}\right)^{\frac{1}{1-\alpha}}, \tag{A3}$$

where ϵ_c is the phase-velocity non-dimensional parameter that reads

$$\epsilon_c = \frac{(\omega')^{\frac{1}{1-\alpha}}}{k'}, \tag{A4}$$

where $\omega' = \frac{z_0}{\beta_0}\omega$ and $k' = z_0 k$. Then, we can express the Rayleigh-wave group velocity as

$$v_u = (\partial_\omega k)^{-1} = \left(\frac{v_c + \frac{\alpha}{1-\alpha}\frac{v_{s,z_0}}{k'}\omega'}{{v_c}^2}\right)^{-1} = (1-\alpha)v_c, \tag{A5}$$

where ∂_ω is the partial derivative along pulsation. Finally, the non-dimensional Rayleigh-wave amplitude N^R reads

$$N^R_{ij} = \frac{2r'_i r'_j}{k'\int_0^\infty (r_1'^2 + r_2'^2)\mathrm{d}z'}, \tag{A6}$$

where $(r'_i)_{i=1,2} = \frac{r_i}{z_0}$ are the non-dimensional horizontal and vertical Rayleigh-wave eigenfunctions and $z' = \frac{z}{z_0}$. To illustrate how the non-dimensional parameters ϵ_c, defined in eq. (A4), and N^R, defined in eq. (A6), change with power α we plot ϵ_c, N^R for the fundamental and the first modes in Fig. A1 for Poisson's ratio $\nu = 0.25$ and a constant quality factor. We observe that the first overtone's non-

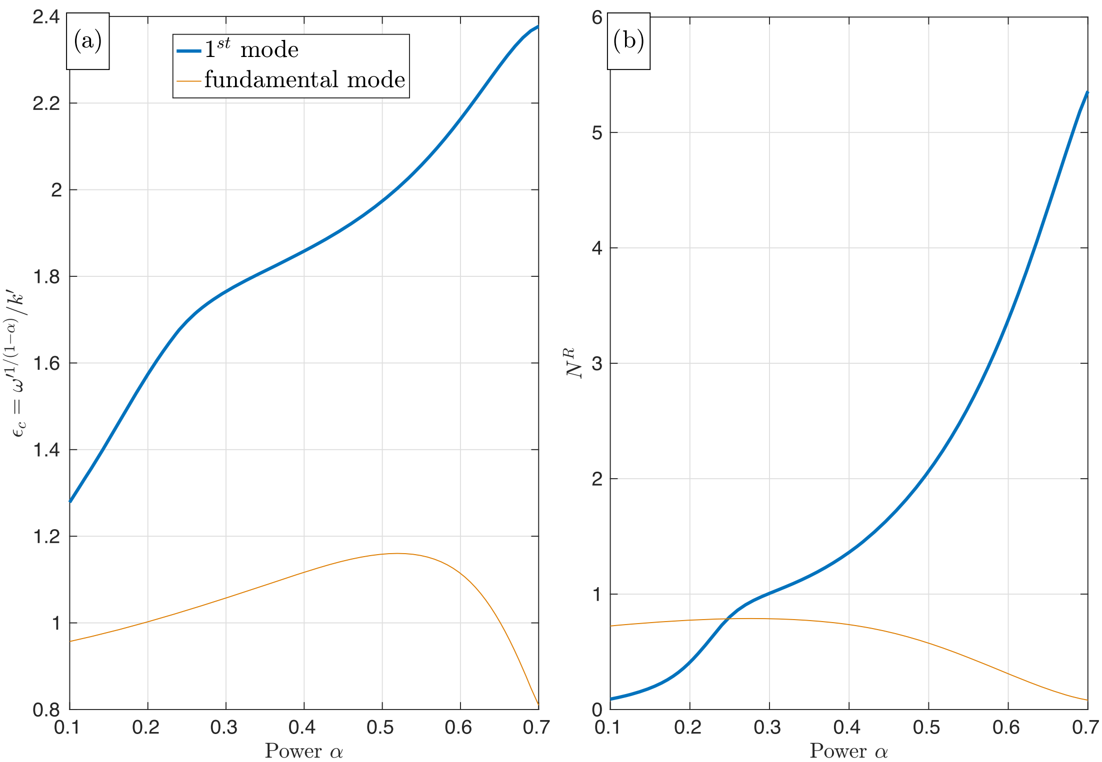

Figure A1. Panel (a), non-dimensional parameter ϵ_c, defined in eq. (A4), for the fundamental mode (the thin orange line) and the first overtone (the thick blue line) against power α for Poisson's ratio $\nu = 0.25$ and no attenuation. Panel (b), non-dimensional parameter N^R, defined in eq. (A6), for the fundamental mode (the thin orange line) and the first overtone (the thick blue line) against power α for Poisson's ratio $\nu = 0.25$ and no attenuation.

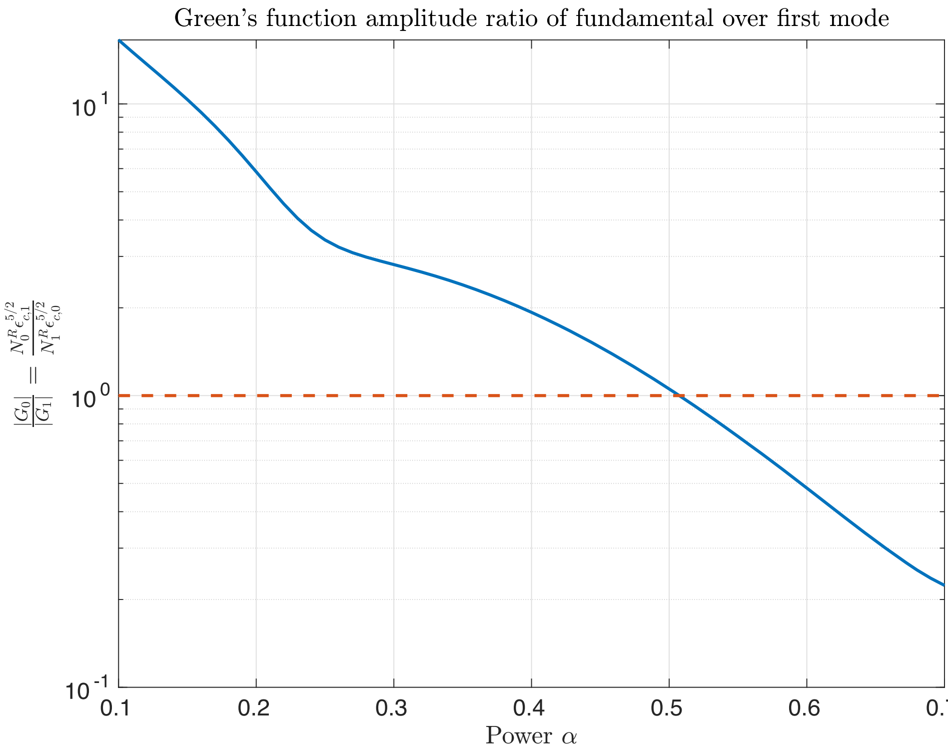

Figure A2. Green's function amplitude ratio against power α of the fundamental mode $|G_0|$ over the first mode $|G_1|$ for Poisson's ratio $\nu = 0.25$ and constant quality factor such that $\frac{|G_0|}{|G_1|} = \frac{N_0^{\mathrm{R}} \epsilon_{c,1}^{5/2}}{N_1^{\mathrm{R}} \epsilon_{c,0}^{5/2}}$, where the subscripts 0 and 1 correspond, respectively, to the fundamental and first Rayleigh-wave mode. The orange dashed line corresponds to $\frac{|G_0|}{|G_1|} = 1$, that is, when the fundamental and the first modes have identical amplitude.

dimensional parameters show significantly larger variations than the ones derived for the fundamental mode. Interestingly, in panel (b), we note that for large α values the non-dimensional amplitude of the first mode becomes larger than the fundamental one.

This is clearly visible in Fig. A2, where we plot the Green's function amplitude ratio of the fundamental mode $|G_0|$ over the first mode $|G_1|$ such that $\frac{|G_0|}{|G_1|} = \frac{N^{\mathrm{R}}{}_0 \epsilon_{c,1}^{5/2}}{N_1^{\mathrm{R}} \epsilon_{c,0}^{5/2}}$. We observe that for $\alpha > 0.4$, the first higher order mode amplitude cannot be neglected as $|G_1| \gtrapprox |G_0|$ for $\alpha > 0.4$.

Finally, from the non-dimensional parameters N_{ij}^{R} and ϵ_{c}, one can compute Green's functions and derive the frequency f_0^r for maximum energy at a distance r for a given constant quality factor Q_{R}. After cumbersome calculations, one obtains

$$f_0^r = \frac{1}{2\pi} \left(\frac{v_{\mathrm{c},0}}{\omega_0^{-1/(1-\alpha)}} \frac{Q_{\mathrm{R}}}{r} (1 + 4\alpha)(1 - \alpha) \right)^{1-\alpha}. \qquad \text{(A7)}$$

In Tsai *et al.* (2012), the authors considered several assumptions to derive a fully analytic model for the phase and group velocities in a power-law medium: $N^{\mathrm{R}} \approx 1$ and the Rayleigh-wave phase velocity decays with depth proportional to e^{-kz} where k is the wavenumber and z is the depth. The method presented in this paper should be preferred as no assumptions are used to derive the Green's functions.

APPENDIX B: PATH EFFECT VELOCITY CORRECTION FROM VISCOELASTIC PROCESSES

To correctly model the energy distribution with Green's functions, one needs to properly account for attenuation. Viscoelastic processes contribute to eq. (2) not only through the quality factor Q_{R} but also through attenuation-induced physical dispersion, that is, the frequency dependence of Rayleigh-wave phase and group velocities. Indeed, low and/or strongly varying quality factors cause significant velocity dispersion (Liu *et al.* 1976). To correct the model for dispersive effects when attenuation is strong, we use the phase velocity correction for Rayleigh waves introduced in Liu *et al.* (1976), which we will refer to as the dispersive path correction (in contrast to the initial non-dispersive velocities). This correction is based on a Zener solid approximation, such that for each frequency, we have $\frac{\Delta v_{\mathrm{c}}}{v_{\mathrm{c},0}} = \frac{1}{\pi Q_{\mathrm{R}}} \ln(\frac{f}{f_m})$, where $\Delta v_{\mathrm{c}} = v_{\mathrm{c}} - v_{\mathrm{c},0}$ is the difference between elastic and viscoelastic phase velocities and f_m is the frequency at which the seismic velocity model is provided. The effect of dispersion on velocity is visible in Fig. B1(a), where we show both the non-dispersive (green) and dispersive (blue) phase velocities against frequency for a given reference frequency $f_m = 0.01$ Hz. In the viscoelastic case, we note that there is a substantial difference between the phase velocities in elastic and viscoelastic media, with phase velocities in the latter case having phase velocity that increases with frequency to the limit $v_{\mathrm{c}} \to 2313\,\mathrm{m\,s^{-1}}$.

In order to study the impact of attenuation-induced dispersion on wave propagation with distance, we focus on the distance-dependent term only by computing the attenuation factor $\gamma(r, f) = e^{-\frac{\pi f r}{v_{\mathrm{u}} Q_{\mathrm{R}}}} / \sqrt{r}$ for the non-dispersive and dispersive cases. We can

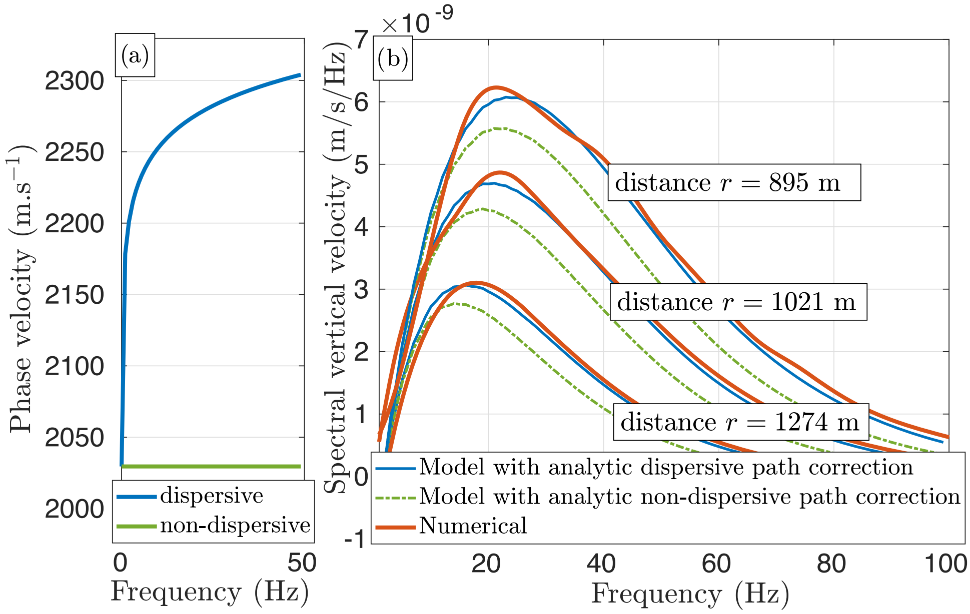

Figure B1. Panel (a), elastic Rayleigh phase velocity profile (green) and viscoelastic Rayleigh phase velocity profile (blue) against frequency for the body-wave quality factors given in Table 1. Panel (b), vertical velocity against frequency from numerical simulations (orange) and the theoretical model with the elastic phase velocity profile (green dashed) and the theoretical model with the viscoelastic phase velocity profile (solid blue) for the simulation parameters presented in Table 1, at various distances from the source $r = 895$, 1021, 1274 m. The theoretical velocity spectra A_{theo} (dashed green and solid blue) are computed from the numerical solution $A_{\mathrm{theo}}(f, r_0)$, at an initial station r_0, such that $A_{\mathrm{theo}}(f, r) = A_{\mathrm{num}}(f, r_0) \times e^{-\pi f |r-r_0|/v_{\mathrm{u}} Q_{\mathrm{R}}} \sqrt{\frac{r_0}{r}}$, where $A_{\mathrm{num}}(f, r_0)$ is the velocity spectrum at the initial receiver location $r_0 = 200$ m.

then express the Green's function solution A_{theo} at distance r from the source as $A_{\mathrm{theo}}(f, r) = \sqrt{r_0} A_{\mathrm{num}}(f, r_0)\gamma(r, f)$, where $A_{\mathrm{num}}(f, r_0)$ is the reference numerical solution at location $r_0 = 200$ m. In Fig. B1(b), we plot the numerical and theoretical vertical velocity spectra, computed with the non-dispersive (referred to as 'non-dispersive path correction') and dispersive (referred to as 'dispersive path correction') phase velocity profiles. We observe that the spectra computed with the non-dispersive elastic velocity do not capture well the amplitude, in this very simple homogeneous case, with an error up to 10 per cent at a distance $r = 1274$ m from the source, while the model with the dispersive path correction has less than 5 per cent error on amplitude and peak frequency. The spectral amplitude without path correction also tends to decrease faster than the numerical solution. This discrepancy comes from the fact that a lower shear-wave group velocity will lead to a lower Rayleigh-wave group velocity and thus a larger value of the attenuation term $e^{-\pi f r/v_{\mathrm{u}} Q_{\mathrm{R}}}$ that will inevitably lead to an overprediction of the viscoelastic dampening.

APPENDIX C: PREDICTIONS OF HIGHER MODE SURFACE WAVES MAIN-FREQUENCY PEAK IN SHEAR-VELOCITY POWER-LAW STRUCTURES

Shear-velocity power-law structures exhibit two main-frequency peaks in their ESDs: The fundamental-mode Rayleigh-wave peak f_0^r and the higher mode frequency threshold f_0. To provide an estimate of the frequency f_0, we ran simulations with the same Poisson's ratio and various α ranging from 0.1 to 0.4. Other simulation parameters are given in Table C1. Results are shown in Fig. C1 from which we were able to express f_0 as $f_0 \approx \frac{1}{2\alpha} f_0^r$, where f_0^r is the surface-wave peak frequency at distance r from the source. Note that f_0^r can be found by finding where the derivative of the surface-wave energy distribution is zero, that is, by solving $\partial_f(E_v(f; x)) = 0$, from eq. (3), for f where ∂_f is the partial derivative along f. In a shear-velocity power-law structure, $E_v(f; x)$ can be analytically derived using the phase and group velocity estimates given in Tsai *et al.* (2012).

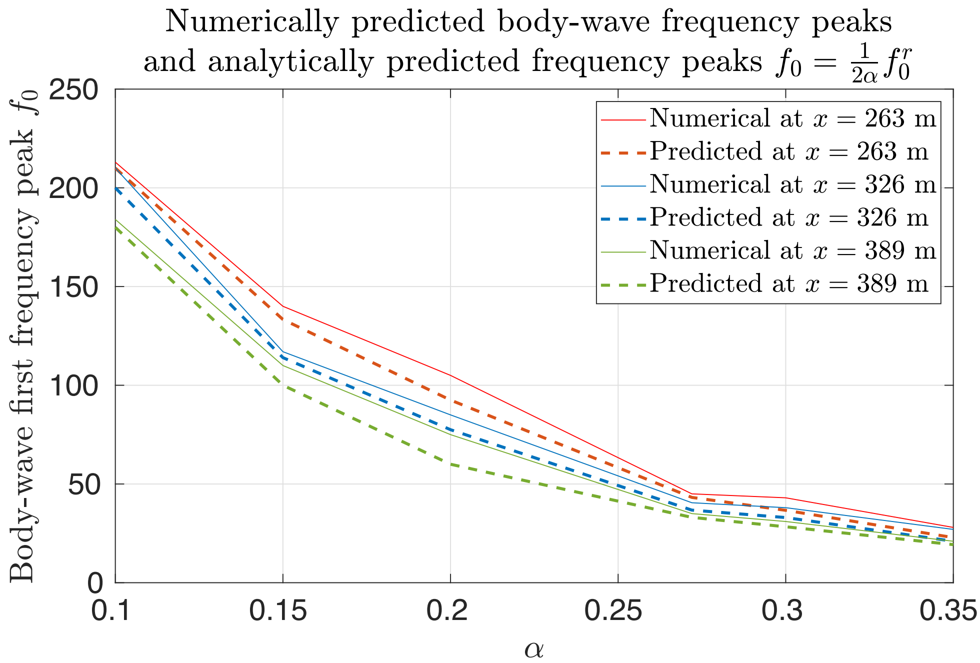

Figure C1. Comparisons between the numerically predicted (dashed) and analytically predicted (solid) higher mode frequency threshold f_0 against α for various distances from the source $r = 263, 326, 389$ m.

Table C1. Simulation parameters for the simulation of seismic waves in a viscoelastic model with a shear velocity power-law structure. L_x and L_z are the horizontal and vertical domain sizes, respectively, ρ is the solid density, α is the shear velocity power-law coefficient, Q_s and Q_p are the shear and compressional quality factors, respectively, and f_0 is the dominant frequency.

$L_x \times L_z$ (m)	ρ (kg m^{-3})	Q_s	Q_p	f_0 (Hz)
1500 × 600	1500	20	40	500